Direct measurements of the stopping power for antiprotons of light and heavy targets

S. P. Møller and E. Uggerhøj
Institute for Storage Ring Facilities, University of Aarhus, DK-8000 Aarhus C, Denmark

H. Bluhme, H. Knudsen, U. Mikkelsen, and K. Paludan
Institute of Physics and Astronomy, University of Aarhus, DK-8000 Aarhus C, Denmark

E. Morenzoni
Paul Scherrer Institute, CH-5232 Villigen PSI, Switzerland
(Received 21 April 1997)

Measurements of antiproton stopping powers around the stopping-power maximum are presented for targets of Al, Si, Ti, Cu, Ag, Ta, Pt, and Au. The Low Energy Antiproton Ring antiproton beam of 5.9 MeV is degraded to 50–700 keV, and the energy loss is found by measuring the antiproton velocity before and after the target. Target thicknesses have been determined accurately by weighing and Rutherford backscattering techniques. The antiproton stopping powers are found to be reduced by around 35% for both light and heavy elements near the electronic stopping-power maximum as compared to the equivalent proton stopping power. The antiproton stopping powers and the Barkas effect; that is, the difference in stopping power between protons and antiprotons is compared to theoretical estimates, based on a harmonic-oscillator model and an electron-gas model, and good agreement is obtained. [S1050-2947(97)09410-9]

PACS number(s): 34.50.Bw, 61.85.+p, 79.20.Rf

I. INTRODUCTION

The stopping power of matter for charged particles is a quantity of large fundamental and applied relevance. The understanding of the slowing down of fast particles in matter has played a significant role in the discoveries and understanding of the constituents of matter ever since the beginning of the century. Generally, it is of great importance to know accurately the stopping power for a broad range of materials in order to interpret a variety of contemporary experiments. For example, ion implantation and ion-beam analysis, which are used extensively today in materials science, require accurate knowledge of stopping powers. The use of proton and heavy ion beams in radiotherapy also relies on this quantity. Experimental stopping powers for protons were reviewed recently [1].

Theoretically, stopping power has been considered since the early days of atomic physics starting with Bohr, Thomson, and Rutherford. The interest was motivated by several factors. It was necessary to have a good theoretical understanding of the stopping process in order to extract information about the atomic particles studied. Furthermore the analysis of penetration phenomena offered a testing ground for the theoretical treatments being developed, starting with classical methods and subsequently turning to quantum-mechanical methods. In this respect, the understanding of stopping phenomena is an iterative dialogue between theory and experiment, as in most areas of physics.

Nevertheless, even today there is good agreement between calculations and experiments only for high energies (the Bethe formula). Around the stopping power maximum, calculations are difficult and only for simple targets like H_2 and He are calculations able to give quantitative results [2]. One general approach to stopping powers involves models, where the stopping material is approximated by simpler systems like an electron gas or sets of harmonic oscillators. The theory for stopping of light ions near the maximum has also been reviewed recently [2].

One of the recent testing grounds of such models is the measurements of the stopping power for antiprotons, or more generally particles of negative charge. This not only allows tests of the models under charge conjugation, i.e., reversal of the sign of the force responsible for the stopping, but the use of negative particles also excludes reaction channels difficult to treat in some models, like electron capture, which contribute significantly to the stopping power for slow protons. In this respect, the antiproton has been named ''the theorist's favorite low-energy projectile'' [3]. Furthermore, the uneven terms in a Born expansion of the stopping power, and in particular the term proportional the cube of the projectile charge, can be elucidated by comparisons of measurements with projectiles of positive and negative charge.

II. BETHE THEORY WITH CORRECTIONS

The collisions between the projectile and the target are usually divided into inelastic collisions, referred to as ''electronic,'' where atoms are excited or ionized, and elastic collisions, referred to as ''nuclear,'' where the atom as a whole recoils. The nuclear stopping only contributes significantly to the stopping power at very low projectile velocities, and can be neglected in the present experiment. For protons, the electronic stopping power has a maximum at a proton velocity corresponding to the typical electron velocity. For lower projectile velocities, the stopping power is approximately velocity proportional as it emerges in an electron-gas calculation, and, above the maximum, the stopping power decreases inversely proportional to the velocity squared as predicted in the first Born approximation. The Bethe formula resulting from this first Born approximation reads [4].

$$-\frac{dE}{dx}=\frac{4\pi e^4 N Z_2}{m\nu^2}Z_1^2 L, \tag{1}$$

where ν is the projectile velocity, N the target density and Z_2 the target atomic number. As a result of the first Born approximation, the stopping power is proportional to the square of the projectile charge Z_1. The Bethe stopping function L, which is independent of Z_1, may be written nonrelativistically as

$$L=\ln(2m\nu^2/I)-C/Z_2. \tag{2}$$

Here I is the so-called mean ionization potential which, together with the so-called shell corrections C/Z_2, is the only quantity depending on the internal structure of the target atoms. The shell corrections originate from the non-negligible target-electron velocities. The mean ionization potential and the shell corrections can only be calculated with reasonable accuracy for the very simplest atoms, and are hence normally extracted from comparisons of the Bethe formula with experimental data.

Formally, one may generalize the Bethe equation to include the higher-order Z_1 terms in the stopping function,

$$L=L_0+Z_1L_1+Z_1^2L_2+\cdots, \tag{3}$$

where L_0, L_1, and L_2 are the Z_1-independent coefficients of the Z_1^2, Z_1^3 and Z_1^4 terms in the stopping power. The same expression also emerges from a Born expansion of the stopping power.

A Z_1^3 (Barkas) correction to the Bethe formula for the harmonic oscillator was first calculated using classical methods by Ashley, Ritchie, and Brandt [5], and by Jackson and McCarthy [6], allowing the target electrons to move during the collision. It was argued that close projectile-electron collisions were essentially collisions between free particles, giving an exact Z_1^2 dependence. Hence the calculation was performed for distant collisions only, with an impact parameter discriminating between close and distant collisions of the order of the radius of the harmonic oscillator. The Jackson and McCarthy result can be written in the form

$$L_1=F(\nu/\sqrt{Z_2}\nu_0)/\sqrt{Z_2}, \tag{4}$$

where $F(x)$ is a numerically given function with a maximum of 0.3 around $x\sim 1$, and where $\nu_0=\alpha c$ is the Bohr velocity, $\alpha\approx 1/137$ being the fine-structure constant.

This distant-collision Barkas effect is related to the polarization of the medium induced by the projectile. This explains qualitatively why negatively charged particles have a lower stopping power than positively charged ones. Such polarization effects are also seen in measurements of single ionization cross sections [7]. Later Lindhard [8] argued that close collisions contribute to the Barkas effect with an equal amount, since the dynamical screening of the projectile charge by the atomic electrons makes the close collisions *deviate* from Coulomb collisions. It was also shown that the Z_1^4 correction (the so-called Bloch term) is as significant as the Z_1^3 correction. The Z_1^4 correction was obtained as the lowest-order term in the difference between the Bethe and the Bloch stopping formulas,

$$L_2=-1.2(\nu_0/\nu)^2. \tag{5}$$

Reviews of the Barkas effect can be found in Refs. [9], [10], and [11].

The deficiencies of the Bethe-Bloch formula (including corrections) lead to the use of models, where the target atoms are modeled by a less realistic system, e.g., an ensemble of harmonic oscillators or an electron gas. The advantage is then that these systems can be treated mathematically with high accuracy and without restrictive approximations. Such model calculations have been used extensively in the qualitative understanding of the slowing-down process. Clearly, the results obtained should be applied quantitatively with caution, since *a priori* it is not clear to what extent such simple systems can describe the properties of real physical systems.

A. Quantal harmonic-oscillator model

The classical harmonic oscillator was used to model the stopping medium, starting with Bohr [12]. Only recently has the quantal harmonic oscillator been treated even in the Bethe theory [13]. Also, higher-order terms have been derived and calculated recently [14]. These calculations are rigorous for the harmonic oscillator, i.e., no approximations are made. Finally, an exact calculation solving the time-dependent Schrödinger equation for the harmonic oscillator has also appeared [15].

The calculations of the stopping properties of the quantal harmonic oscillator are carried out in the straight-line trajectory approximation as a function of impact parameter. Hence Coulomb deflection effects are ignored, and consequently the results are not applicable at very low energies. These calculations result in a significant contribution to the Z_1^3 term for *all* impact parameters, thus supporting Lindhard's argument that close collisions also contribute to the Z_1^3 term. In the present context, we are only interested in the average stopping power corresponding to integration over all impact parameters.

For the harmonic oscillator, L_0, L_1 and L_2 are calculated numerically as function of the scaled energy variable $2m\nu^2/\hbar\omega$. The tabulated values of L_0, L_1 and L_2 are given in units of $(\nu_0/\nu)^0$, $(\nu_0/\nu)^1$, and $(\nu_0/\nu)^2$, respectively, in Refs. [13] and [14]. Since this is an experimental paper, we will not reproduce the theoretical result in these variables, but instead we compare L_0, L_1, and L_2 for the M shell in silicon in Fig. 1 in the energy region 20–4000 keV relevant for the present experiment. We point out here that the absolute value of L_2 is shown, since it it positive at small energies and turns into the Bloch expression $-1.2(\nu_0/\nu)^2$ in the large energy limit. We note the decrease of L_1 and L_2 with increasing energy, as compared to the slow logarithmic increase in L_0 reflecting the improved accuracy of the Bethe formula for high energies.

In Fig. 2 we plot L_0, L_1 and L_2 for the K, L and M shell in silicon as function of energy. Furthermore the total values of L_0, L_1, and L_2 are presented. The total values of L_n are in the harmonic-oscillator model calculated as

$$L_n=\sum w_{i0}L_n\left(\frac{E_i-E_0}{\hbar}\right), \tag{6}$$

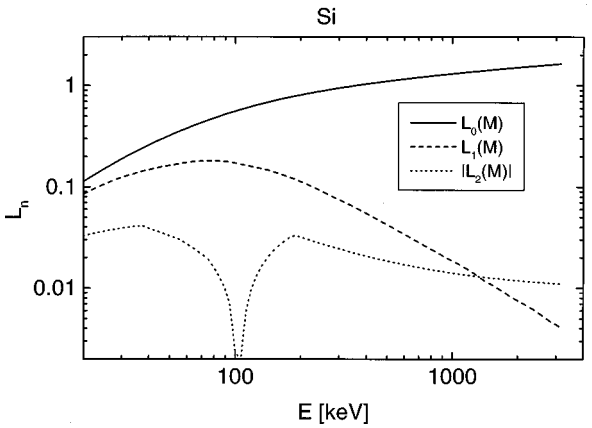

FIG. 1. Z_1^2, Z_1^3, and Z_1^4 terms L_0 (solid curves), L_1 (dashed curves), and L_2 (dotted curve) calculated using the harmonic-oscillator model for the M shell in silicon.

where E_i is the energy of the ith excitation states and w_{i0} are the dipole oscillator strengths from the ground state, and where $L_n(\omega)$ is the L_n value of the spherical, harmonic oscillator with a resonance frequency ω. Some of the elements used in the present experiment, Al, Si, Cu, Ta, Pt, and Au, are modeled by a number of harmonic oscillators corresponding to the atomic shells. The oscillator energies and strengths used are given in Table I. These values are obtained from shell-wise integration of the oscillator strengths given in Ref. [16]. These oscillator strengths and energies also satisfy the sum rules

$$\sum w_{i0}=1, \quad \ln I=\sum w_{i0} \ln E_i, \tag{7}$$

In Fig. 2 we observe that in the low-energy region the energy loss in silicon is dominated by the M shell, whereas in the high-energy region both the L and M shells are significant. Even at the highest energies considered in this plot, the K-shell contribution is at the level of a few percent. At the highest energies in the plot, L_1 contributes around 2% to the energy loss, whereas at the lowest energies the corresponding number is 60%. For L_2, the contribution to the energy loss is around 0.3% and 25% at high and low energies, respectively.

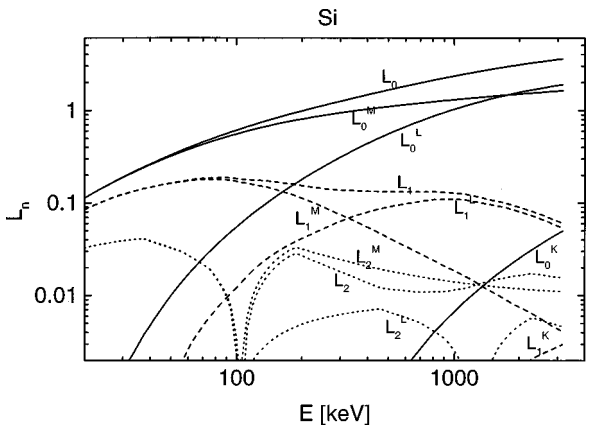

FIG. 2. Z_1^2, Z_1^3, and Z_1^4 terms L_0 (solid curves), L_1 (dashed curves), and L_2 (dotted curves), calculated using the harmonic-oscillator model for the K, L, and M shells in silicon. Also, the total values of L_0, L_1, and L_2 are shown.

TABLE I. Oscillator strengths w and energies E used in the harmonic-oscillator model calculations.

	Al	Si	Cu	Ta	Pt	Au
w_K	0.1349	0.1222	0.0505	0.0126	0.0129	0.0139
E_K (keV)	2.795	3.179	16.931	88.926	95.017	96.235
w_L	0.6387	0.5972	0.2561	0.0896	0.0745	0.0803
E_L (keV)	0.202	0.249	1.930	18.012	25.590	25.918
w_M	0.2264	0.2806	0.4913	0.2599	0.2295	0.2473
E_M (keV)	0.0169	0.0203	0.199	3.210	4.063	4.116
w_N			0.2021	0.3413	0.4627	0.423
E_N (keV)			0.0396	0.575	0.576	0.599
w_O				0.2057	0.1324	0.1124
E_O (keV)				0.1087	0.0819	0.0873
w_P				0.0908	0.0879	0.1231
E_P (keV)				0.0308	0.0314	0.0369
I (keV)	0.164	0.168	0.322	0.709	0.764	0.800

The lowest-order term L_0 in the stopping power for silicon, represented by the same ensemble of harmonic oscillators, is shown in Fig. 3 together with the stopping powers based on $L_0+L_1+L_2$ and $L_0-L_1+L_2$ corresponding to the stopping powers for protons and antiprotons. This figure reveals the Barkas effect, i.e., the difference between the stopping power for protons and antiprotons. We see that the Barkas effect is a very significant effect at the stopping power maximum and below, which means that higher-order terms are needed at these energies in order to get a good estimate of the stopping power.

B. Electron-gas model

Another model that has been extensively used in calculations of stopping powers is the electron-gas model, in which case the target electrons are described as an electron gas of varying complexity. An electron gas is expected to represent

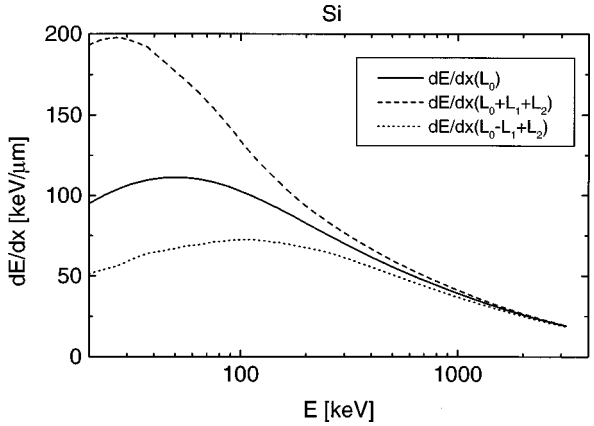

FIG. 3. The lowest-order term, the Z_1^2 term, in the stopping power for silicon in the harmonic-oscillator model (solid curve), is here compared to the stopping power for protons (dashed curve) and antiprotons (dotted curve) calculated by inclusion of the Z_1^3 and the Z_1^4 terms.

a metallic target very well at low energies, since here only valence electrons (conduction electrons) contribute to the stopping; see Fig. 2. A recent calculation, valid for low projectile velocities, appeared in Ref. [17] using a degenerate, homogenous Fermi gas. Here the stopping power emerges as

$$-\frac{dE}{dx}=\frac{4}{3\pi}Z_1^2C(\chi)\,\frac{v}{v_0}\,\frac{e^2}{a_0^2}, \tag{8}$$

where the density parameter is given as $\chi=(v_0/\pi v_F)^{1/2}$ and where the Fermi velocity is given by the electron density n, $v_F=(3\pi^2 n)^{1/3}\hbar/m$. The Bohr radius a_0 is given as $a_0=\hbar^2/me^2$. The stopping function C is only dependent on the density parameter χ *and* Z_1. We observe a velocity proportional stopping power. The actual stopping power for a given material can subsequently be found in the local-density approximation by averaging C over the actual electron densities encountered in the target.

The stopping function C was calculated in Ref. [17] in different approximations for different values of χ, i.e., different electron densities, for protons and antiprotons. First, an analytical second-order Born expression for C is given as $C=C_1+C_2$, where C_1 is independent of Z_1 and C_2 is proportional to Z_1. The second-order term C_2 appears to be only slightly lower than C_1, and hence even a second-order Born approximation seems too crude for an accurate estimate of the stopping power. Hence a self-consistent quantum-mechanical calculation was performed in Ref. [17]. The stopping powers found for protons and antiprotons are then $\langle C\rangle\approx 0.9\langle C_1\rangle$ and $\langle C\rangle\approx\langle C_1+3C_2/2\rangle$, respectively, where the averages refer to the local-density approximation, and where C_1 and C_2 refer to the second-order Born calculation. The results for antiprotons are expected to be quite reliable, whereas the results for protons are more problematic owing to the problems of electron capture. The first order results obtained in Ref. [17] are $\langle C_1\rangle=0.31$, 0.30, 0.28, 0.39, 0.40, and 0.38 for Al, Si, Ge, Cr, Cu, and Ag, respectively. We notice here the very weak dependence of the electron-gas calculation to the electron density; the density actually appears in the stopping power to the power $\frac{1}{6}$ in a logarithm.

A calculation of the Barkas term for energy loss in an electron gas in the high-energy region has also appeared [18]. Here solid silicon is represented as a *static* electron gas both for the local-density case and for the homogeneous case.

III. INTRODUCTION TO EXPERIMENTS

For positive particles, a large amount of experimental data is available at energies both below and above the stopping-power maximum [1]. Deviations from a Z_1^2 scaling of the stopping power were first signaled from observed range differences between positive and negative pions of equal velocity [19]. The idea that this range difference originated from a difference in stopping power for positive and negative particles was, however, not obvious [20]. Later these departures were also seen using beams of sigma hyperons and pions [20,21]. However, the experiments suffered from the low quality of the secondary beams used.

Deviations from a pure Z_1^2 scaling of the stopping power will also show up in comparisons of stopping powers for light, bare nuclei. This deviation was first observed by Andersen *et al.* [22] in comparisons between stopping powers for protons and α particles. Later lithium nuclei were also included as projectiles [23], whereby it became possible to extract the Z_1^2, Z_1^3, and Z_1^4 terms in the stopping power (neglecting higher-order terms). Such measurements of the higher-order terms are restricted to the high energies (>1 MeV/amu) owing to electron-capture effects for the lithium nuclei. However, many measurements of the Z_1^3 term have over the years been derived from proton and α particle measurements assuming the Z_1^4 term to be given by the Bloch term, Eq. (5).

Clearly, such experiments do not directly prove the existence of a close-collision contribution to the Barkas effect, and although, e.g., the measurements made by Andersen *et al.* essentially agreed with Lindhard's assessment, equally good agreement was obtained by Ritchie and Brandt [24] without recourse to a close-collision contribution by adjustment of the impact-parameter cutoff.

For negative particles, several more or less indirect stopping power measurements have been made after the initial experiments by Barkas and co-workers. These measurements have been performed using muons in solids [25] and in light gases [26], and antiprotons in light gases [27]. The stopping powers in these experiments were derived from the obtained distribution of slowing-down times, possibly combined with simultaneous projectile-range distributions. Trial functions for the stopping power are used to simulate these distributions, which subsequently are compared to the experimental distributions. Furthermore, several experimental corrections are made in these experiments.

In contrast to those measurements, the present experiment is direct, in the sense that the stopping power is obtained from a measured change in velocity of the projectiles due to their penetration of a target of known thickness, and measures as such directly ''the decrease of velocity of moving electrified particles on passing through matter'' described by Bohr in 1913 [12]. These measurements are an extension of a previous demonstration of the time-of-flight technique in combination with a degraded antiproton beam [28], and part of the data have already been published in a recent letter [29]. Time-of-flight techniques are usually not used for stopping power measurements in the 10–1000-keV regime, since high-quality beams of protons and other ions are readily available, and hence more accurate methods exist. However, it seems to be the best choice for the antiproton beam of 5.9 MeV available.

We have previously also used the antiproton beam from the Low-Energy Antiproton Ring (LEAR) at CERN to measure the Barkas effect in silicon via a comparison of stopping powers for protons and antiprotons accurately [30,31]. The method developed was limited to silicon, since the energy loss was inferred from the energy deposited in an active silicon detector. Owing to the difficulties inherent in the production of thin detectors, this method cannot easily be extended to energies below 200 keV. However, it was also used at higher energies (up to 3 MeV), where the short flight times make the present time-of-flight technique inaccurate.

IV. EXPERIMENTAL METHOD

The present experiment used a 5.9-MeV antiproton beam from LEAR with an intensity around 10^5/s. As shown in Fig.

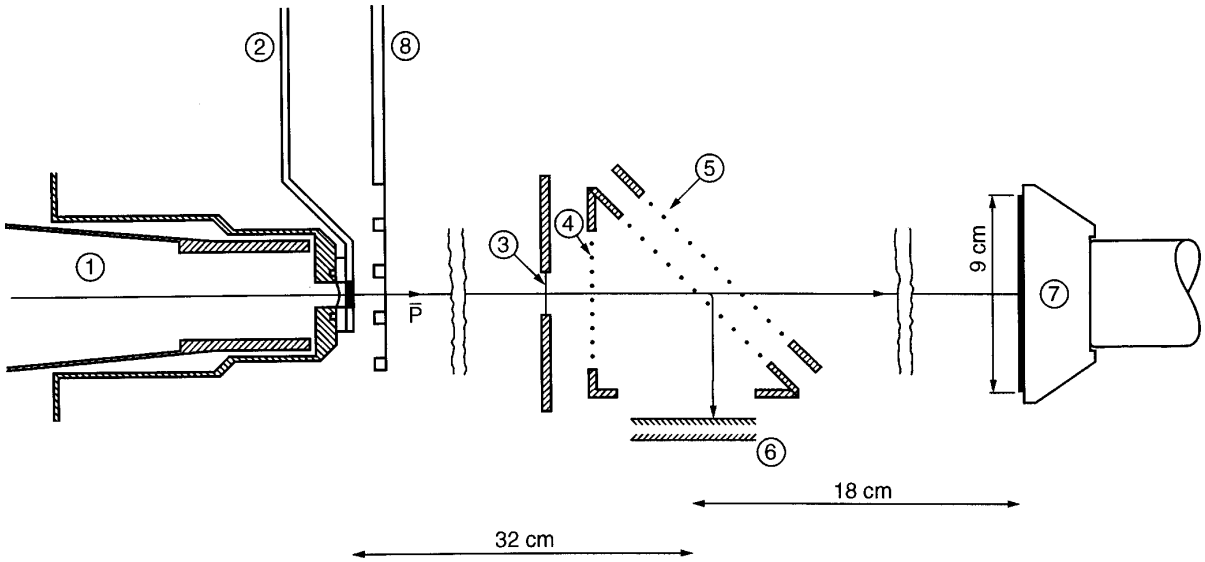

FIG. 4. Schematic drawing of the experimental setup. The numbers refer to (1) beam line vacuum chamber with beryllium window, (2) start scintillator, (3) absorber foil, (4) and (5) electrical mirror, (6) channel-plate detector, (7) stop scintillator, and (8) target ladder with degrader foils.

4, the beam exits the LEAR vacuum system through a 100-μm beryllium window (1) and enters after passing 1 cm of air the experimental-vacuum chamber through a 20-μm mylar foil. Here the beam traverses a 100-μm scintillator (2) before passing the degrader consisting of beryllium foils (8); beryllium is chosen to reduce multiple scattering, and hence increase the count rate. The degrader foils were mounted on a turnable target ladder with four positions containing (1) no degrader (resulting in an energy of 2.53 MeV), (2) 25-μm Be (giving 1.96 MeV), (3) 50-μm Be (giving 1.31 MeV), and (4) 50-μm Be and 5-μm Al (giving 1.05 MeV). By turning this last degrader 45°, we obtained a beam with energies between roughly 50 and 700 keV. After the degrader and the first flight path, the beam traversed the target foil (3) whose stopping power was to be measured, and the beam was finally stopped in the stop scintillator (7) after the second flight path. Since both the incident and exit energies are required, we measure the time of flight (TOF) of the particles from the 100-μm-thick start scintillator to the absorber foil and from the foil to the 1-mm-thick stop scintillator. The data, i.e., the two TOF times together with the amplitudes of the signals and other relevant information, are accumulated on an event-by-event basis using a CAMAC system connected to a personal computer. The timing signal from the absorber foil is obtained from the emitted secondary electrons. These electrons are accelerated from the foil (3) reflected by an electrical mirror (5) and further accelerated towards a micro-channel plate detector (6), Fig. 4.

The time resolution as obtained with the high-energy beam of 2.53 MeV is 1.1 and 0.7 ns (rms) on the incident and exit sides respectively. This corresponds to an energy resolution of 1.5 keV at 100 keV. Several important measures were needed to obtain this resolution. First of all, well-adjusted constant-fraction discriminators were used to reduce time jitter from varying pulse heights. Furthermore, the main degrader was placed after the first scintillator to achieve a small spread in the pulse heights from this scintillator. Finally, the energy deposited in the last scintillator varied from a few tens of keV to a few tens of MeV owing to the annihilation products from the annihilating antiproton. Hence the timing resolution could be improved considerably with a rather high discriminator level for this last scintillator, corresponding to a few MeV. Clearly, this led to a reduction in the efficiency.

Standard delays were used to calibrate the time-to-digital converters (TDC's). The energies of the four monoenergetic degraded beams obtained with the four degraders described above were deduced from flight times measured for two different flight paths differing by a well-known distance of around 0.5 m. Finally, the two calibration constants were obtained by a fit to these four energies and the corresponding TDC channel numbers. Drift in the timing was checked repeatedly during the experiment via measurements of the TOF peaks without degrader. The drifts observed were up to 0.4 ns during the whole run, and are the major contributor to the uncertainty in the TOF determination.

The total efficiency of the system is rather low (10^{-4}–10^{-5}), owing to the low efficiency of the secondary electron detection (a few percent), the high-energy cut on the last scintillator, and also because of the large multiple scattering of the antiprotons when they are degraded to energies below 1 MeV.

The targets used in the experiment were 0.3–3-μm foils of Al, Si, Ti, Cu, Ag, Ta, Pt, and Au. The thicknesses of the foils have been measured carefully by weighing and by Rutherford backscattering (RBS) using 2-MeV α particles, and 1.2-MeV protons for the very thickest foils. As an example, in Fig. 5 we show the RBS spectrum for the 0.36-μm Al target together with a simulation of the same spectrum. The two small peaks to the left stem from oxygen on the two surfaces. The uncertainty in the RBS measurements are less

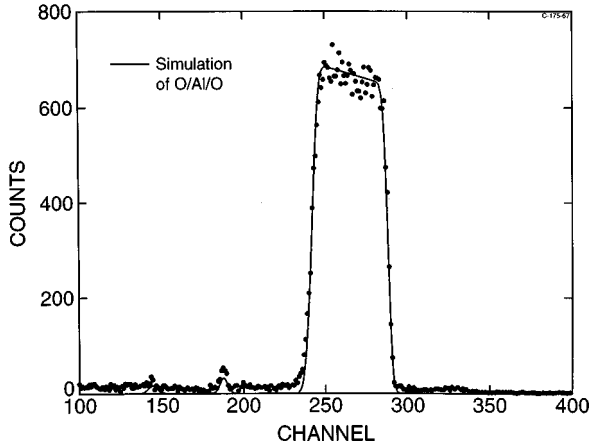

FIG. 5. Rutherford backscattering plot for the 0.36-μm Al target.

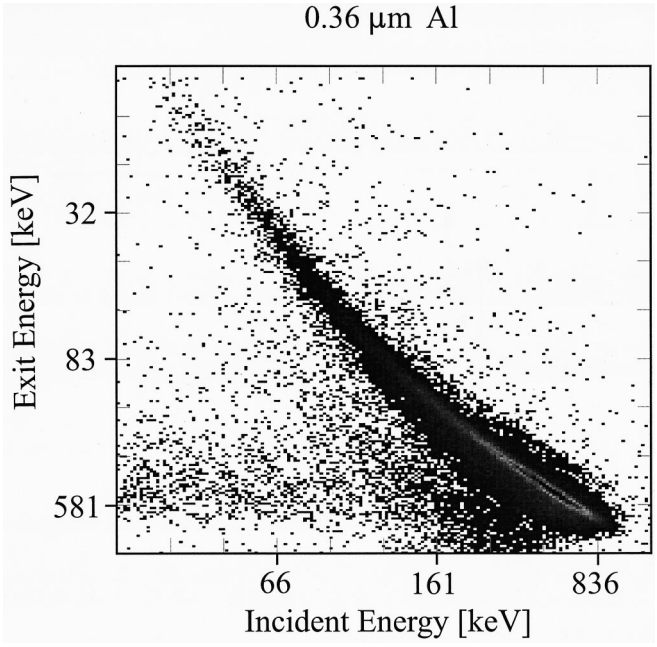

FIG. 6. Scatter plot of the two time-of-flight times for the degraded beam used, and for the 0.36-μm Al absorber foil.

than ± 100 Å for thin foils, and ± 200 Å for thick foils, whereas the uncertainty in the weighing procedure is considerably larger. The two methods give consistent results within the uncertainties, but significant deviations from the thicknesses specified by the manufacturer were found. The results of the foil-thickness determinations are given in Table II.

Using the degrader consisting of 50-μm beryllium and 5-μm aluminum turned 45°, a beam with energies between 50 and 700 keV is obtained. For illustration, in Fig. 6 we show a scatter plot of the two flight times for the degraded beam and for the 0.36-μm Al target. A small background from accidentials are seen together with the ''banana''-shaped distribution. Three incident and exit energies are marked. ''Monoenergetic'' beams are then selected in the analysis by software cuts on the incident TOF. The stopping power is subsequently determined as $dE/dx=\Delta E/\Delta x=(E_1-E_2)/\Delta x$ at the energy $E_1-\Delta E/2$, where E_1 is the incident energy, E_2 is the exit energy and Δx the absorber thickness.

TABLE II. Measured thicknesses of the foils used in the experiment.

Element	Weighted thickness (μm)	Nominal thickness (μm)	RBS thickness (μm)
Al	0.52	0.30	0.36
Al	0.68	0.80	0.63
Al	3.30	3.00	3.78
Si		0.50	0.48
Ti	0.85	0.80	0.84
Ti	2.11	2.50	2.08
Cu	0.34	0.50	0.33
Cu	2.44	2.00	2.33
Ag	0.75	0.50	0.55
Ag	2.09	2.00	1.90
Ta	1.45	1.50	1.43
Ta	2.62	2.50	2.87
Pt	1.40	1.25	1.40
Pt	2.56	2.50	2.60
Au	0.37	0.50	0.31
Au	1.95	2.00	2.05

V. RESULTS

Figures 7(a)–7(h) show that the measured antiproton stopping power for the eight different elements used. The error bars correspond to an uncertainty of 0.5 ns in the determination of the TOF, and a 200-Å uncertainty in the thickness of the foils used. This gives rise to an uncertainty increasing with impact energy owing to the decreasing TOF and energy loss. Hence this uncertainty is systematic and not statistical, as also reflected in the scatter of the data. Statistical errors contribute much less. Only measurements with total uncertainties less than 25% are plotted.

Solid targets are inevitably crystalline/polycrystalline, and directional effects, channeling, are known to alter the energy loss drastically for positive particles. Hence we have also checked for directional effects in the energy loss of antiprotons, but the result was negative. It should be mentioned that channeling effects exist for antiprotons, as seen in transmission experiments [32].

First we give some comments relating to the previous measurements on silicon and gold. Our previous data for Au [28] show stopping powers slightly lower than the present results. Motivated by the discrepancies found in the present experiment between the specified and the actual thicknesses of our targets, we also measured the thicknesses of the foils used in the first experiment. The thicknesses were found to be up to 17% thinner than specified by the manufacturer, which brings the results into agreement with the present results. These old data have been renormalized according to these new thickness measurements, and included in Fig. 7(h). Also the silicon data are consistent with the old data [30,31] in the overlap region, although the old data seem to extrapolate to lower values than the new measurements. This is pre-

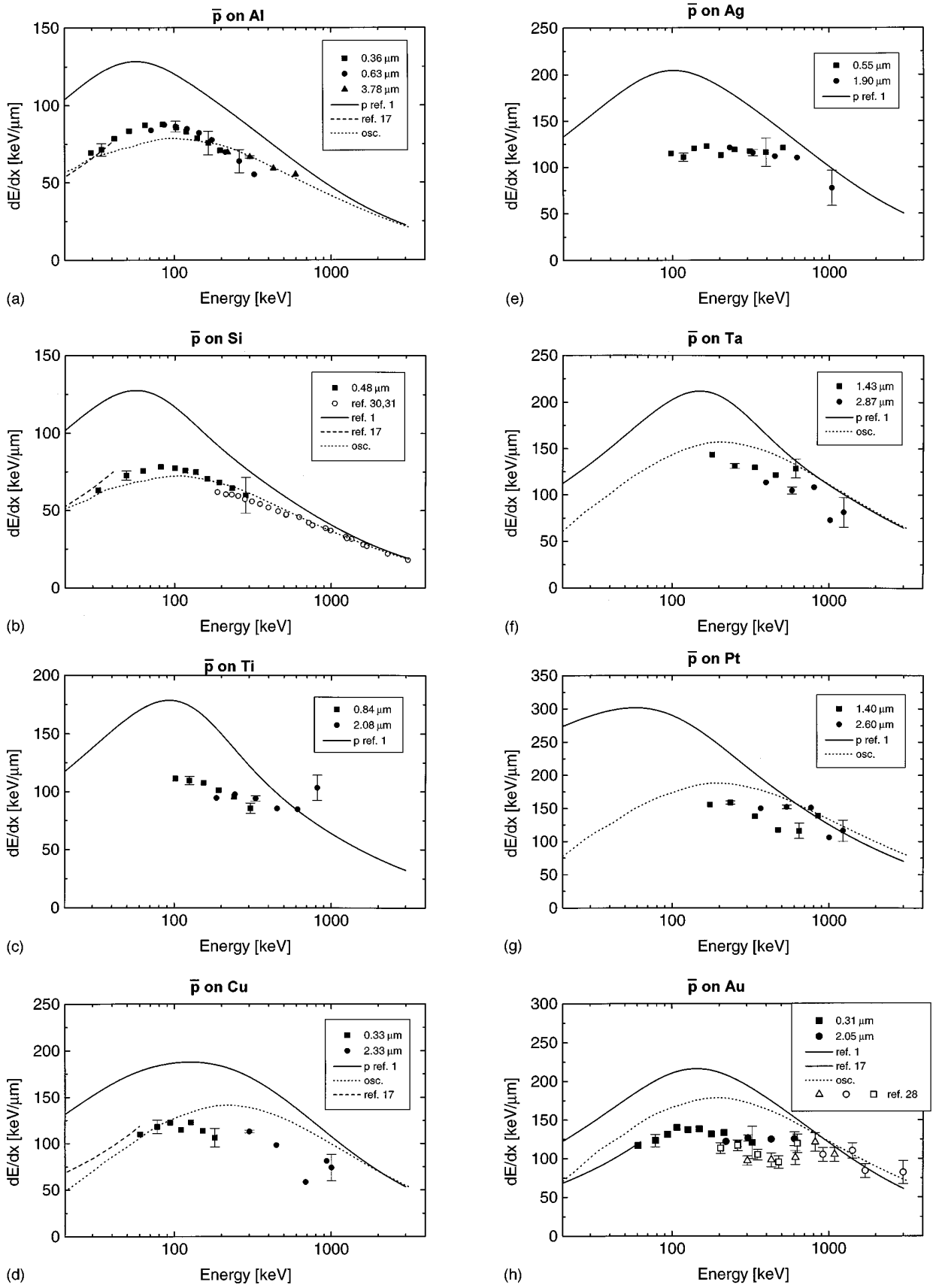

FIG. 7. Measured antiproton-stopping power, ■, ●, and ▲ in aluminum (a), silicon (b), titanium (c), copper (d), silver (e), tantalum (f), platinum (g), and gold (h) compared to proton data [1] (full-drawn curves). The dashed curves are the antiproton-stopping powers predicted by the electron-gas model [17]. The dotted curves are the antiproton-stopping powers predicted by the harmonic-oscillator model. The open symbols, □, △, and ○, in (b) and (h) are from our previous LEAR experiment, Refs. [30], [31] and [28], respectively.

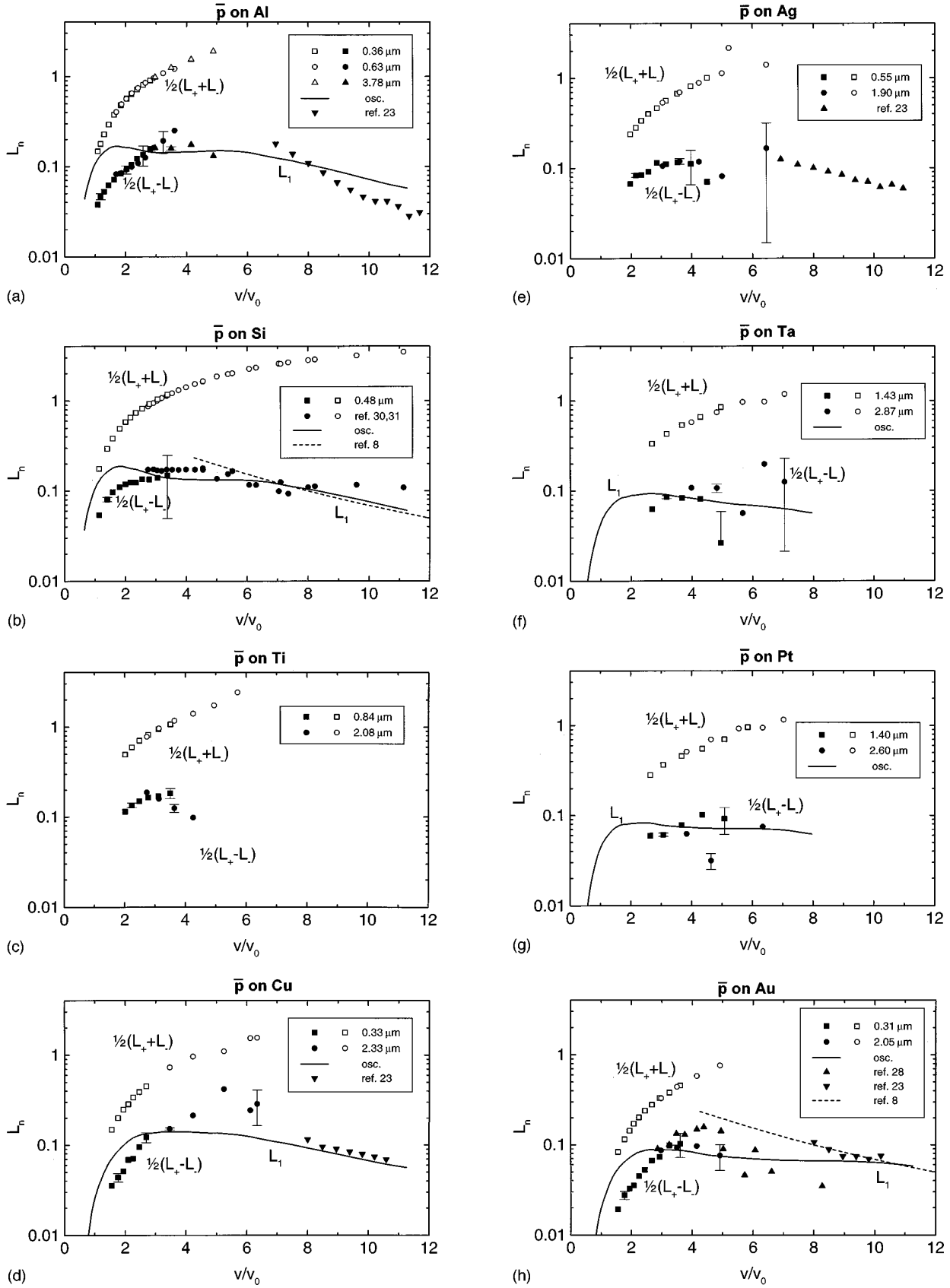

FIG. 8. Extracted values for $\frac{1}{2}(L_+ - L_-)$, ■, ●, and ▲, and $\frac{1}{2}(L_+ + L_-)$, □, ○, and △, for aluminium (a), silicon (b), titanium (c), copper (d), silver (e), tantalum (f), platinum (g), and gold (h) as functions of velocity relative to the Bohr velocity. The circles in (b), ● and ○, and the filled up-triangles ▲ in (h) are from our previous LEAR experiment, Refs. [30], [31], and [28], respectively. The full-drawn curves are the result of the oscillator-model calculation for L_1, whereas the dashed lines are the Lindhard estimate, Ref. [8]. Finally, the filled down triangles (▼) are from Ref. [23].

sumably due to a systematic error in the energy calibration, but we point out that the discrepancies are well within the error bars. We also remark that these previous measurements were obtained using active silicon detectors, where the energy loss is inferred from the energy deposited in the target. Finally, we observe that results for a given element from foils of different thickness merge well in the overlap regions.

The foils used have a diameter of 15 mm, and cover scattering angles (in the start scintillator and the degrader) less than 1°, whereas a beam degraded to an energy of around 0.5 MeV has an angular spread of several degrees (rms). On the exit side of the foils, the stop scintillator accepts scattering angles less than 14°. This relatively small acceptance angle, less than the multiple scattering angle for the lowest energies, ensures that angle-dependent effects and corrections from the difference between the actual path length of the projectiles and the target thickness, the projected path length, can be neglected.

All proton-stopping powers shown in Fig. 7 are from Ref. [1]. The present data exhibit a stopping power maximum for antiprotons, which for Al and Si appears at a slightly higher energy than for protons. For Cu, Ag, and Au a rather flat maximum is seen. For Ti, Ta, and Pt, the foils used were too thick for stopping-power measurements at or below the maximum. The antiproton stopping power around the maximum appears to be reduced, as compared to protons, by 30–40% for all materials.

The stopping power for antiprotons from the harmonic-oscillator model, described in Sec. II A, are calculated for the Al, Si, Cu, Ta, Pt, and Au targets and plotted on the corresponding figures. We observe, that for the light targets, Al and Si, the model reproduces the measurements very well on the high-energy side of the maximum. For the same targets, the model calculations, however, gives a maximum of the right value but at too high an energy. For the heavy elements, Cu, Ta, Pt, and Au, the model does not even reproduce the measurements at high energy. We also point out that the same harmonic-oscillator model overestimates the stopping power for protons with around 50% for all targets.

The data for Si, Al, Cu, and Au are also compared to the electron-gas model, as described in Sec. II B. The electron-gas calculation is only plotted for energies below the maximum, where the stopping power seems to be velocity proportional. The electron-gas calculation gives very good agreement with the measurements at the lowest energies attainable.

Another way of relating the experimental data with theory is to compare the difference in the experimental stopping power between protons and antiprotons with the theoretically obtained Z_1^3 term, L_1. Neglecting terms of order higher than 3, L_1 can be extracted as half the difference between the stopping functions for protons (L_+) and antiprotons (L_-), i.e., $L_1=\frac{1}{2}(L_+-L_-)$. In Figs. 8(a)–8(h), the deduced values of $\frac{1}{2}(L_+-L_-)$ are shown for all the targets, together with $\frac{1}{2}(L_++L_-)$, which represents L_0+L_2. The proton stopping function L_+ is extracted from Ref. [1]. Error bars stemming from the uncertainties on the antiproton measurements are drawn on the extracted values of $\frac{1}{2}(L_+-L_-)$. We have also shown the value of $\frac{1}{2}(L_+-L_-)$ deduced from the old antiproton measurements, Refs. [28], [30], and [31], and using the new proton stopping powers from Ref. [1].

In Fig. 8, for Al, Si, Cu, Ta, Pt, and Au, we have also plotted the result from the oscillator model. These theoretical calculations are slightly different from those used in Ref. [29] based on the same model. The reason is that another set of oscillator strengths and energies, which are believed to better than those used in Ref. [29], are used in this paper. Also the old estimate by Lindhard of the L_1 term is shown in Figs. 8(b) and 8(h). We see that this estimate agrees quite well with the experiment and the oscillator model at high velocities. Also, at lower velocities, the oscillator calculations reproduce the experimental values remarkably well for all targets, although the decrease in L_1 appears at a lower velocity in the model than the experimental $\frac{1}{2}(L_+-L_-)$. This could be due to the poor convergence of the Born series at low energies. The high-energy measurements of L_1 from Ref. [23] are also shown in the figure, and they agree very well with the model calculations.

We notice that the agreement between calculated and experimental stopping powers is much better for antiprotons than for protons for both the harmonic-oscillator and electron-gas models. This can, at least partly, be explained by the absence of electron capture for negative particles, since electron capture is not included in any of the models. Furthermore we point out that the results for the harmonic-oscillator model depend on the convergence of the Born series. This convergence is known to be slow at low velocities [15].

VI. CONCLUSIONS

In conclusion, accurate direct measurements of the stopping power for antiprotons around the stopping power maximum have been presented for several targets. The maximum stopping power for antiprotons is found to be around 65% of the equivalent stopping power for protons for both light and heavy elements. The harmonic-oscillator model seems to reproduce the measured stopping powers for the light elements. The stopping-power measurements at very low energy are seen to agree with the asymptotic behavior calculated in the electron-gas model. Above the stopping power maximum, the Barkas effect (or the L_1 term) is well reproduced by the oscillator model calculation, but the strong decrease in the Barkas term seen experimentally occurs at a higher energy than in the model. An extension of the presently used technique to even smaller energies seems feasible. This would allow a test of the velocity proportionality of the stopping power at low energies for negatively charged particles. The present low-energy antiproton beams will, however, not be available after the closure of LEAR at the end of 1996.

ACKNOWLEDGMENTS

We are grateful to Henning H. Mikkelsen for providing the oscillator strengths and oscillator energies used in the harmonic-oscillator model calculations. We also appreciate the discussions with Henning H. Mikkelsen and Allan H. Sørensen on the issues discussed in the present paper.

[1] ICRU Report No 49, ISBN 0-913394-47-5, 1993 (unpublished).
[2] P. Sigmund, Nucl. Instrum. Methods Phys. Res. B **85**, 541 (1994).
[3] A. H. Sørensen, Phys. At. Nucl. **57**, 1758 (1994).
[4] H. A. Bethe, Ann. Phys. (Leipzig) **5**, 325 (1930). U. Fano, Annu. Rev. Nucl. Sci. **13**, 1 (1963).
[5] J. C. Ashley, R. H. Ritchie, and W. Brandt, Phys. Rev. B **5**, 2393 (1972); Phys. Rev. A **8**, 2402 (1973).
[6] J. D. Jackson and R. L. McCarthy, Phys. Rev. B **6**, 4131 (1972).
[7] P. Hvelplund, H. Knudsen, U. Mikkelsen, E. Morenzoni, S. P. Møller, E. Uggerhøj, and T. Worm, J. Phys. B **27**, 925 (1994).
[8] J. Lindhard, Nucl. Instrum. Methods **132**, 1 (1976).
[9] H. Bichsel, Phys. Rev. A **41**, 3642 (1990).
[10] G. Basbas, Nucl. Instrum. Methods Phys. Res. B **4**, 227 (1984).
[11] H. H. Andersen, in *Semiclassical Descriptions of Atomic and Nuclear Collisions*, edited by J. Bang *et al.* (Elsevier, New York, 1985), p. 409.
[12] N. Bohr, Philos. Mag. **25**, 10 (1913).
[13] P. Sigmund and U. Haagerup, Phys. Rev. A **34**, 892 (1986); H. H. Mikkelsen and P. Sigmund, Nucl. Instrum. Methods Phys. Res. B **27**, 266 (1987).
[14] H. H. Mikkelsen and P. Sigmund, Phys. Rev. **40**, 101 (1989); H. H. Mikkelsen, Nucl. Instrum. Methods Phys. Res. B **58**, 136 (1991); Radiat. Eff. Defects Solids **126**, 63 (1993).
[15] H. H. Mikkelsen and H. Flyvbjerg, Phys. Rev. A **45**, 3025 (1992).
[16] *Handbook of Optical Constants of Solids*, edited by Edward D. Palik (Academic, New York, 1985).
[17] A. H. Sørensen, Nucl. Instrum. Methods Phys. Res. B **48**, 10 (1990).
[18] H. Esbensen and P. Sigmund, Ann. Phys. (N.Y.) **201**, 152 (1990).
[19] W. H. Barkas, W. Birnbaum, and F. M. Smith, Phys. Rev. **101**, 778 (1956).
[20] W. H. Barkas, N. J. Dyer, and H. H. Heckman Phys. Rev. Lett. **11**, 26 (1963).
[21] H. H. Heckman, and P. J. Lindstrom, Phys. Rev. Lett. **22**, 871 (1969).
[22] H. H. Andersen, H. Simonsen, and H. Sørensen, Nucl. Phys. A **125**, 171 (1969).
[23] H. H. Andersen, J. F. Bak, H. Knudsen, and B. R. Nielsen, Phys. Rev. A **16**, 1929 (1977).
[24] R. H. Ritchie and W. Brandt, Phys. Rev. A **17**, 2102 (1978).
[25] W. Wilhelm, H. Daniel, and F. J. Hartmann, Phys. Lett. **98**, 33 (1981); W. Schott, H. Daniel, F. J. Hartmann, and W. Neumann, Z. Phys. A **346**, 81 (1993); P. Wojciechowski *et al.*, Hyperfine Interact. **82**, 127 (1993).
[26] F. Kottmann, in *Proceedings of the 2nd International Symposium On Muon and Pion Interactions with Matter (Dubna, 1987)*, edited by V. P. Dzelepov (Joint Institute for Nuclear Research, Dubna, 1987), p. 268; P. Hauser, F. Kottmann, Ch. Lüchinger and R. Schaeren, in *Muonic Atoms and Molecules*, edited by L. A. Schaller and C. Petitjean (Birkhäuser Basel, 1993) p. 235; F. Kottmann, in *Proceedings of the International School of Physics of Exotic Atoms*, edited by C. Rizzo and E. Zavattini (INFN, Trieste, 1994), p. 297.
[27] A. Adamo *et al.*, Phys. Rev. **47**, 4517 (1993); M. Agnello *et al.*, Phys. Rev. Lett. **74**, 371 (1995).
[28] R. Medenwaldt, S. P. Mølerr, E. Uggerhøj, T. Worm, P. Hvelplund, H. Knudsen, K. Elsener, and E. Morenzoni, Phys. Lett. A **155**, 155 (1991).
[29] S. P. Møller, E. Uggerhøj, H. Bluhme, H. Knudsen, U. Mikkelsen, K. Paludan, and E. Morenzoni, Nucl. Instrum. Methods Phys. Res. B **122**, 162 (1997).
[30] L. H. Andersen, P. Hvelplund, H. Knudsen, S. P. Møller, J. O. P. Pedersen, E. Uggerhøj, K. Elsener, and E. Morenzoni, Phys. Rev. Lett. **62**, 1731 (1989).
[31] R. Medenwaldt, S. P. Møller, E. Uggerhøj, T. Worm, P. Hvelplund, H. Knudsen, K. Elsener, and E. Morenzoni, Nucl. Instrum. Methods Phys. Res. B **58**, 1 (1991).
[32] S. P. Møller, E. Uggerhøj, J. Bluhme, H. Knudsen, U. Mikkelsen, K. Paludan, and E. Morenzoni (unpublished).